Low-Frequency Mean Square Slopes and Dominant Wave Spectral Properties: Toward Tropical Cyclone Remote Sensing

Paul A. Hwang and Yalin Fan

***Abstract*— Spectral properties near the dominant wave region influence significantly the surface roughness relevant to ocean remote sensing employing low-frequency microwave sensors. The critical parameters characterizing dominant waves are wind speed and dimensionless spectral peak frequency, which is the inverse wave age. The dimensionless spectral peak frequency can be expressed as an equivalent dimensionless fetch or duration. The connection between dominant waves and surface roughness is the spectral slope. This paper presents a surface wave spectral model designed for low-frequency microwave remote sensing, with special emphasis on tropical cyclone (TC) applications. The key elements of the spectral model are: 1) a general spectral function with coefficients accommodating a variable spectral slope and 2) a parametric function connecting the spectral slope and wind speed, which is established with the mean square slope (MSS) observations obtained inside hurricanes by the global positioning system reflectometry technique. In order to make use of the MSS observations inside hurricanes, parametric models of the spatial distributions of wind speed and dimensionless spectral peak frequency inside TCs are developed. The parametric models are based on the wind and wave similarity relationships derived from analyses of hurricane hunter measurements.**

***Index Terms*— Hurricane, mean square slope (MSS), remote sensing, wave spectrum.**

I. Introduction

THE surface roughness properties relevant to microwave ocean remote sensing are closely related to the sensor frequency and the primary mechanisms responsible for the microwave signal return. For example, Bragg resonance is critical to scatterometry operating at moderate incidence angles and the important surface roughness elements are distributed in a narrow surface wave spectral region satisfying the resonance condition defined by the microwave wavelength and the local incidence angle at the ocean surface. The length scales of these resonance surface wave components (Bragg waves) are typically much shorter than the dominant surface waves near the wave energy spectral peak. The local wind dependence of Bragg waves is strong, and dominant waves make only minor modification of the resulting scattering return.

Manuscript received April 23, 2018; revised May 23, 2018; accepted June 23, 2018. This work was supported by the Office of Naval Research under Grant N0001416WX00044. *(Corresponding author: Paul A. Hwang.)*

P. A. Hwang is with the Remote Sensing Division, U.S. Naval Research Laboratory, Washington, DC 20375 USA (e-mail: paul.hwang@nrl.navy.mil).

Y. Fan is with the Oceanography Division, U.S. Naval Research Laboratory, Stennis Space Center, Bay St. Louis, MS 39529 USA (e-mail: yalin.fan@nrlssc.navy.mil).

Color versions of one or more of the figures in this paper are available online at http://ieeexplore.ieee.org.

Digital Object Identifier 10.1109/TGRS.2018.2850969

In contrast, titling is critical to reflectometry and the roughness elements are low-pass-filtered surface waves several times longer than the microwave wavelength. Obviously, the dominant wave influence grows stronger as the microwave frequency decreases. The connection between the dominant waves and the surface roughness is the spectral slope.

Several milestones marking the long effort of spectral model development of wind-generated waves are Pierson and Moskowitz [1], referred to as the P model; Hasselmann *et al.* [2], [3], referred to as the J model [for Joint North Sea Wave Project (JONSWAP)]; and Donelan *et al.* [4], referred to as the D model. These spectral models prescribe a constant spectral slope ($-s$) in the high-frequency region: -4 for the D model and -5 for P and J models.

Field observations [5], [6], however, show that s varies over a rather wide range. Young [5], referred to as the Y model, incorporates a variable s in the spectral function. The Y model, however, does not resolve the spectral slope dependence of the associated spectral coefficients, and its application relies on the spectral coefficients developed by the D or J spectral model, so its legitimate use remains for -4 or -5 slope.

In a recent analysis of the directional wave spectra observed inside hurricanes by an airborne scanning radar altimeter system during several National Oceanic and Atmospheric Administration (NOAA) hurricane reconnaissance and research missions, it is concluded that s needs to be treated as a stochastic random variable with a mean value near 4.5. The hurricane wave spectral analyses lead to the development of a general surface wave spectral model (the G model) with the associated coefficients accommodating a variable spectral slope [6]. Because the wave height determination is relatively insensitive to the high-frequency components of the wave spectrum, the mean s value and its dependence on the wind and wave properties cannot be obtained from analyzing the surface elevation spectrum. A detailed review of the wind wave spectral models discussed above is given in [6]. A concise version summarizing the mathematical formulas is given in the Appendix.

With the G model, we explore in Section II the impact of spectral slope on the resulting low-pass-filtered mean square slope (LPMSS) computation. The analysis leads to the conclusion that it is critical to develop a function describing the dependence of the representative spectral slope, i.e., the mean s, on wind and/or wave properties. From this point, the term spectral slope or the variable s refers to the mean value of the stochastic s variable.

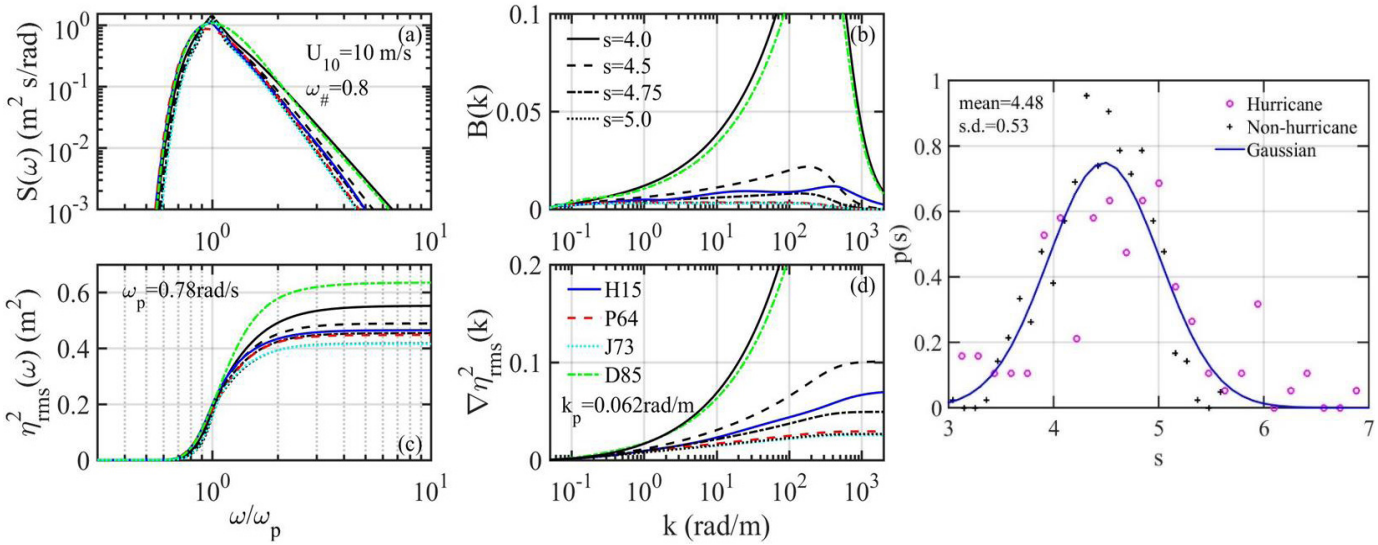

Fig. 1. Example of the wave spectra computed with different spectral slopes ($-s$) in the high-frequency region. (a) Wave elevation frequency spectrum $S(\omega)$. (b) Wave slope spectrum given in terms of the dimensionless wavenumber spectrum $B(k)$. (c) Cumulative surface elevation variance plotted against dimensionless frequency (normalized by the spectral peak frequency). (d) Cumulative mean square surface slope variance. Black curves show the G spectra [6] for four different s values, color curves show the P [1], J [2], [3], D [4], and H [11] spectra, and further detail is given in the legend. (e) pdf of s in field observations under hurricane (magenta markers) and nonhurricane (blue markers) conditions; the superimposed curve is the Gaussian distribution with mean and standard deviation shown at the upper left corner.

Interest in ocean remote sensing using the L-band microwaves from global positioning system (GPS) has resulted in an expansive collection of LPMSS measurements; many of the data were obtained in hurricanes [7]–[10]. These LPMSS measurements provide a great opportunity to quantify the dependence of the spectral slope on various wind and wave properties. In order to make use of these LPMSS data, we need to derive an understanding of the general properties of winds and waves inside hurricanes.

Recent analyses of winds and waves measured in hurricane reconnaissance and research missions have revealed several interesting similarity relationships of surface waves generated by hurricane wind fields. Of particular importance to the wave spectral modeling is the similarity relations of surface wind speed U_{10} and the dimensionless spectral peak frequency $\omega_{\#} = \omega_p U_{10}/g$, where g is the gravitational acceleration, ω is the surface wave angular frequency, subscript p indicates the spectral peak component, and subscript # represents dimensionless quantities. Parametric models are developed to describe the spatial distributions of U_{10} and $\omega_{\#}$ inside hurricanes making use of the similarity relationships (Section III). With the help of the parametric models, the LPMSS data from GPS reflectometry are then used to formulate a functional relationship between s and U_{10}.

Section IV shows the results of modeling the LPMSS inside hurricanes and the comparison with field measurements by GPS reflectometry. Section V is a summary.

II. Wave Spectral Slope and Surface Roughness

Fig. 1 shows an example of the computed wave frequency spectra $S(\omega)$ based on the G model for $U_{10} = 10$ m/s in fully developed sea ($\omega_{\#} = 0.83$) and $s = 4, 4.5, 4.75$, and 5 (black curves). The mathematical equations of the G spectral function and the associated spectral coefficients are given in (A14)–(A20). Superimposed for comparison with colored curves are the results of P [1], J [2], [3], and D [4] models. (The mathematical formulas of the P, J, and D models are also given in the Appendix.) The result from a surface roughness model built on the similarity relationship of short scale waves combining *in situ* ocean measurements and inversion of global data of backscattering normalized radar cross sections at L-, C-, and Ku-bands is also shown, reported by Hwang and Fois [11] and represented as the H model here. The significant impact of the spectral slope on the high-frequency wave components is easily detectable.

The impact is especially striking in terms of the surface slope. The dimensionless wavenumber spectra $B(k) = k^3 S(k)$, corresponding to the wave elevation spectra displayed in Fig. 1(a), are shown in Fig. 1(b), where k is the wavenumber ($2\pi/\lambda$, λ is the wavelength). The connection between wavenumber and wave frequency spectra is

$$S(\omega)d\omega = S(k)dk. \tag{1}$$

The wave dispersion relationship connects ω and k. For waves longer than a few centimeters, the gravity wave dispersion relationship applies

$$\omega^2 = gk. \tag{2}$$

In the semilogarithmic presentation displayed in Fig. 1(b), the area under the $B(k)$ curve for a given wavenumber range is the integrated mean square slope (MSS) of the specified wavenumber components. The cubic wavenumber weighting in $B(k)$ or the quadratic weighting on the slope spectrum $S_{\nabla\eta}(k) = k^2 S(k)$ highlights the dominant contribution of short wave components to the ocean surface roughness, which is frequently represented by the MSS.

The impacts of spectral slope on the spectral contents of wave height and surface roughness are further investigated with the cumulative spectral variance of surface displacement (wave height) and surface slope. For the displacement variance $\eta^2_{\rm rms}$ [Fig. 1(c)], the high-frequency short waves make only negligible contribution. The cumulative displacement variance essentially reaches its maximum at approximately $\omega = 2$–$4\ \omega_p$. For the given example, 2–4 ω_p is 4–16 k_p, or wavelengths 25.3–6.3 m [$\omega_p = 0.78$ rad/s and $k_p = 0.062$ rad/m are printed in Fig. 1(c) and (d)].

In contrast, for the slope variance $(\nabla\eta)^2_{\rm rms}$, the energetic wave components near the spectral peak region contribute very little, and the magnitude of shortwave contribution depends strongly on the wave spectral slope [Fig. 1(d)].

Because the scattering or emission of electromagnetic (EM) waves from the ocean surface is critically modified by the surface roughness condition, the correct specification of the surface wave spectral slope is an important subject for the geoscience remote sensing of the ocean using microwave techniques. Fig. 1(e) shows the spectral slope probability distribution function (pdf) derived from observations in hurricane and nonhurricane conditions. The spectral slope is determined by the spectral components between $2\omega_p$ and $4\omega_p$. The hurricane data were from an analysis of hurricane-generated directional wave spectra recorded by ocean buoys and collected over a 16-year period off the northwest coast of Australia [12]. Many of the spectral slopes fall between -3 and -6; the mean value is -4.56. The nonhurricane data are from an air–sea interaction experiment conducted in the Gulf of Tehuantepec, Mexico, under conditions of strong mountain gap winds; the waves were recorded with fast-response wire gauges [13]–[15]. The spectral slopes analyzed in both hurricane and nonhurricane conditions show a similar Gaussian distribution given as the blue solid curve in Fig. 1(e).

Attempts to correlate s with various wind and wave parameters did not yield a concrete result. The wind and wave parameters explored include surface wind speed U_{10}, significant wave height H_s, dominant wave period T_p, their dimensionless combinations $\eta_\# = \eta^2_{\rm rms} g^2/U^4_{10}$, $\omega_\# = \omega_p U_{10}/g$, and several swell–sea ratios, the root-mean-square (rms) wave elevation $\eta_{\rm rms}$ is related to the significant wave height by $H_s = 4\eta_{\rm rms}$, and the angular frequency of the spectral peak component ω_p is $2\pi/T_p$. It is deduced that s needs to be treated as a stochastic random variable [6]. The mean value of s is neither -4 nor -5 as specified in the widely used wind wave spectral models (see [1]–[4]). This is the main reason for developing the G spectral model that accommodates a variable spectral slope. The G model offers an opportunity for us to evaluate quantitatively the effect of s on the surface roughness relevant to low-frequency microwave applications, i.e., the LPMSS.

One of the earliest efforts to quantify the LPMSS in the ocean is given by Cox and Munk [16]. They conducted photographic measurements of sun glitters from aircraft in clean and slicked water surfaces. The artificial slicks they produced on the ocean surface suppressed waves shorter than about 30 cm.

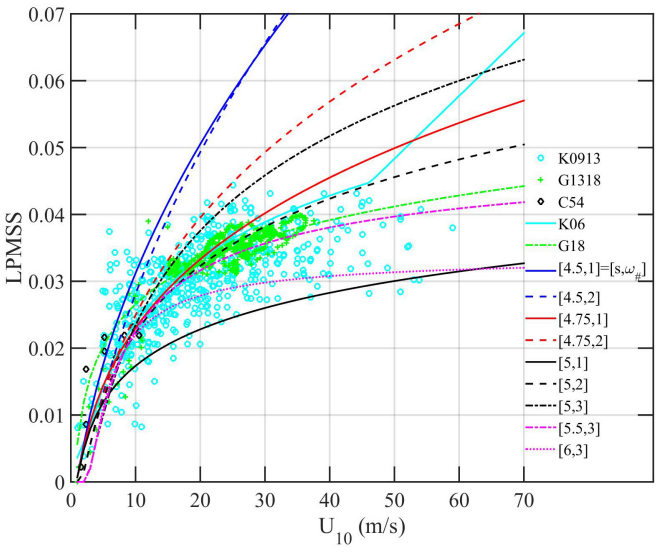

Fig. 2. LPMSS observed in the ocean from sun glitter analysis (black markers) in artificial-slicked water [16] and GPS reflectometry technique: K0913 (cyan markers) is from [7] and [8], and G1318 (green markers) is from [9] and [10]. The cyan curve (K06) is from [17], and the green curve (G18) is from [10]. The remaining curves are computations using the G-spectrum model with [s, $\omega_\#$] values given in the legend for each curve.

GPS reflectometry provides the largest amount of LPMSS measurements to date; many of the data were collected inside hurricanes. Fig. 2 shows the results reported in [7]–[10], together with the analysis result of airborne sun glitter measurements in artificial slick ocean surfaces (black diamonds, labeled C54) reported in [16]. For convenience, in the remainder of this paper, data from [7] and [8] are designated the K0913 group, and those from [9] and [10] are G1318. For K0913, the ocean surface wind speeds are from airborne dropsondes, and for G1318, they are from stepped frequency microwave radiometer (SFMR) and ocean buoys. When clarification is necessary, these LPMSS derived from GPS reflectometry is denoted by $\rm MSS_{GPS}$ in this paper. The spaceborne remote sensing expands the wind speed range considerably.

The K0913 data, shown with cyan circles, are digitized from [7, Figs. 1 and 2] and [8, Figs. 8(b) and 9(b)]; those figures display the GPS-derived wind speeds versus the dropsonde winds. The LPMSS is then calculated with their formula relating the LPMSS and wind speed as described in [17, eqs. (3) and (4)], or in [8, eqs. (5) and (6)], the latter set corrects a typographic error in the former set. The computation using the formula is shown with the cyan solid line in the figure (labeled K06).

The G1318 data, shown with green pluses, are obtained from [9, Table 2], which lists the LPMSS and buoy U_{10}, and digitized from [10, Fig. 13], which gives LPMSS versus SFMR wind speed. The best-fit formula described in [10] is shown with green dashed-dotted line in the figure (labeled G18).

Using the G-spectrum model, we can compute the LPMSS for any combination of U_{10}, $\omega_\#$, and s. Several examples are illustrated in Fig. 2, showing the LPMSS (low-passed at $k = 10$ rad/m) versus U_{10}; the two numbers in square brackets in the figure legend are s and $\omega_\#$ for each curve.

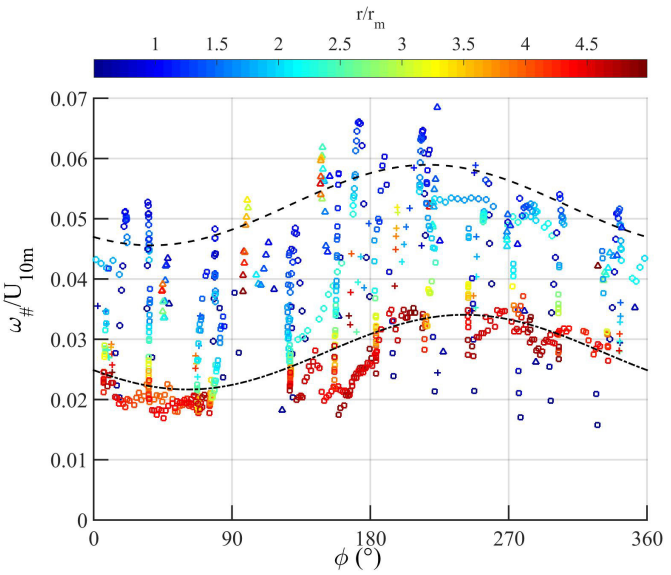

Fig. 3. Azimuthal and radial variations of $\omega_\#$ combining data from four hurricane reconnaissance and research missions. The normalization factors used in this figure are U_{10m} and r_m for $\omega_\#$ and r, respectively.

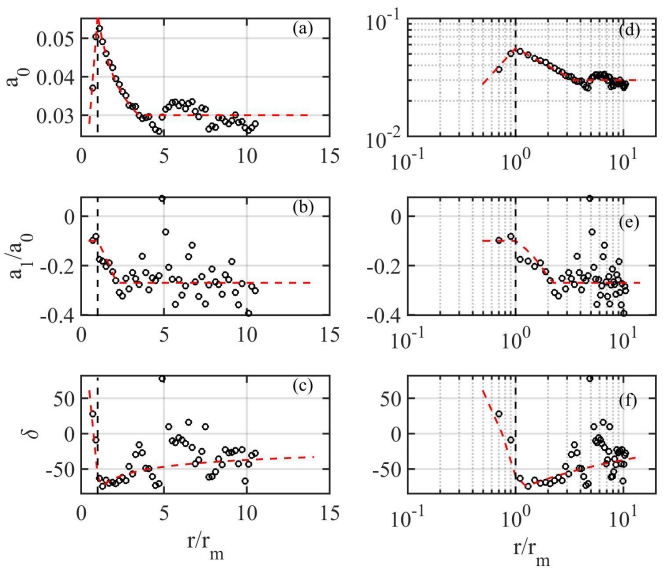

Fig. 4. Coefficients of the parametric model (3) describing the azimuthal and radial variations of $\omega_\#$ shown in Fig. 2; the superimposed red dashed lines are approximation functions given in (4)–(6). The results are shown in linear scales in the left column and logarithmic scales in the right column. (a) and (d) a_0. (b) and (e) a_1/a_0. (c) and (f) δ.

When clarification is necessary, this LPMSS derived from the G spectral model for matching the GPS reflectometry data is denoted by MSS_{k10} in this paper.

The G spectral model results show the significant impacts of s and $\omega_\#$ for quantifying the relationship between LPMSS and U_{10}, especially in high winds. In low and moderate winds (U_{10} less than about 10 m/s), the envelopes formed by $[s,\ \omega_\#] = [4.5,\ 1]$ and $[5,\ 1]$ serve as the approximate upper and lower bounds of the expected wind sea contribution. Measurements outside the envelopes are likely from nonlocal-wind effects such as high swells and sea slicks, in addition to the measurement uncertainty. The results show the importance of incorporating the s and $\omega_\#$ factors for interpreting the $\mathrm{MSS}_{\mathrm{GPS}}$ measurements from the ocean.

Recent analyses of wind and wave measurements obtained by hurricane hunters have shown some useful similarity relationships of the spatial distributions (radial and azimuthal variations) of winds and waves inside tropical cyclones (TCs) [6], [18]–[20]. Making use of these similarity properties, in Section III, we describe parametric models of U_{10} and $\omega_\#$ inside hurricanes. These parametric models are crucial for the computation of LPMSS under TC wind forcing conditions. The $\mathrm{MSS}_{\mathrm{GPS}}$ data will be revisited for deriving a U_{10} dependence of the s factor (Section IV) with the help of the U_{10} and $\omega_\#$ parametric models.

III. Parametric Models of Hurricane Wind Speed and Dimensionless Spectral Peak Frequency

The systematic spatial variation of $\omega_\#$ inside hurricanes has been described in detail in [20]. Combining measurements from four hurricane scenes (categories 2–5) analyzed in [20], Fig. 3 shows the azimuthal distribution of $\omega_\#$; the plotting marker is color-coded with the radial distance r from the hurricane center. The azimuth angle ϕ is measured from the hurricane heading and positive counterclockwise. For the present analysis, we use the hurricane maximum wind speed U_{10m} and radius of maximum wind speed r_m as the normalization factors for $\omega_\#$ and r, respectively; i.e., the normalized variables are $\omega_* = \omega_\#/U_{10m}$ and $r_* = r/r_m$. The prominent feature of $\omega_*(\phi)$ is the sinusoidal variation

$$\omega_* = a_0(r_*) + a_1(r_*)\cos[\phi + \delta(r_*)]. \tag{3}$$

The coefficients a_0, a_1, and δ vary with r_* as shown in (3) explicitly. Two examples are illustrated with smooth curves in Fig. 3. They are generated by fitting through data within $0.85 \le r_* \le 1.15$ (top curve) and $3 \le r_* \le 5$ (bottom curve). Least-squares fitting of the data within narrow r_* bins ($\Delta r_* = 0.2$) produces the coefficients a_0, a_1, and δ shown in Fig. 4, in linear scales in the left column and logarithmic scales in the right column. The general trends are outlined with red dashed lines in Fig. 4

$$a_0 = \begin{cases} 0.0056 r_*, & r_* \le 1 \\ 0.0056 r_*^{-0.5}, & 1 < r_* \le 3.3 \\ 0.03, & 3 < r_* \end{cases} \tag{4}$$

$$\frac{a_1}{a_0} = \begin{cases} -0.1, & r_* \le 1 \\ -0.1 r_*^{-1/3}, & 1 < r_* \le 2 \\ -0.27, & 2 < r_* \end{cases} \tag{5}$$

$$\delta = \begin{cases} -60 + 240(1 - r_*), & r_* \le 1.1 \\ -80 r_*^{-1/3}, & 1.1 < r_*. \end{cases} \tag{6}$$

Equation (3), with coefficients (4)–(6), is the parametric model of ω_* inside hurricanes.

The modified Rankine vortex model described in [21] and [22] is used as the foundation of the wind speed parametric model. To account for the wind field asymmetry, we employ $U_{10m\phi}$, the maximum wind speed along a radial

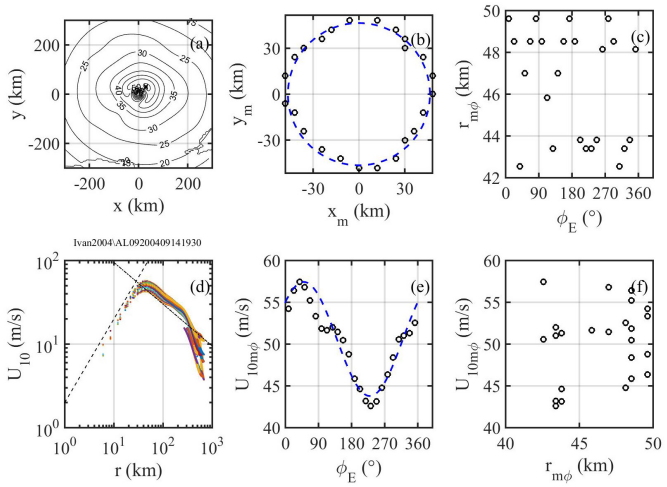

Fig. 5. Example of the HWIND analysis for developing the parametric model of hurricane wind fields (7). (a) Contour map of U_{10}. (b) Coordinates of the maximum wind locations (x_m, y_m) at various azimuth angles. (c) Azimuthal variation of $r_{m\phi}$. (d) Radial variation of wind speed; the slopes of the superimposed power-law line segments are 1 and −0.5. (e) Azimuthal variation of $U_{10m\phi}$. (f) Scatterplot of $U_{10m\phi}$ and $r_{m\phi}$.

transect with a given ϕ, as the normalization factor

$$\frac{U_{10}(r,\phi)}{U_{10m\phi}} = \begin{cases} r_*, & r_* \le 1 \\ r_*^{-0.5}, & 1 < r_*. \end{cases} \tag{7}$$

This formulation assumes a circular eyewall. Noncircular eyewalls can be accommodated by using an azimuthally varying radial distance of maximum wind speed $r_{m\phi}$. (See further discussion in the following.)

The following formula is used for $U_{10m\phi}$:

$$\frac{U_{10m\phi}}{U_{10m}} = 1 - a_{1U}[1 - \cos(\phi - \phi_m)] \tag{8}$$

where U_{10m} is the (overall) maximum wind speed and ϕ_m is the azimuth angle of the U_{10m} location. From examining the archived NOAA HWIND 2-D wind fields in several historical hurricanes, a_{1U} is found to vary mostly between about 0.1 and 0.2, and ϕ_m is mostly in the right-hand side relative to the hurricane heading, with higher probability in the right-front quadrant (ϕ between 270° and 360°) than the right-back quadrant (ϕ between 180° and 270°). An example of the analysis is given in Fig. 5. The 2-D wind field is displayed in Fig. 5(a); the radial dependence of wind speed [Fig. 5(d)] follows closely the modified Rankin vortex model (7) for the r range between about 0 and 300 km; the slopes of the superimposed line segments in Fig. 5(d) are 1 and −0.5. The result of $r_{m\phi}$ analysis is shown in Fig. 5(b) and (c); no clear azimuthal dependence is found. In contrast, the prominent sinusoidal azimuthal dependence of $U_{10m\phi}$ is shown in Fig. 5(e). Fig. 5(f) illustrates a relatively weak correlation between $U_{10m\phi}$ and $r_{m\phi}$. In the remainder of this paper, $r_{m\phi} = r_m$, ϕ_m between 250° and 290°, and a_{1U} between 0.05 and 0.25 are used for presenting the computation results. These parameter ranges are selected based on examining the historical 2-D wind fields of the HWIND product.

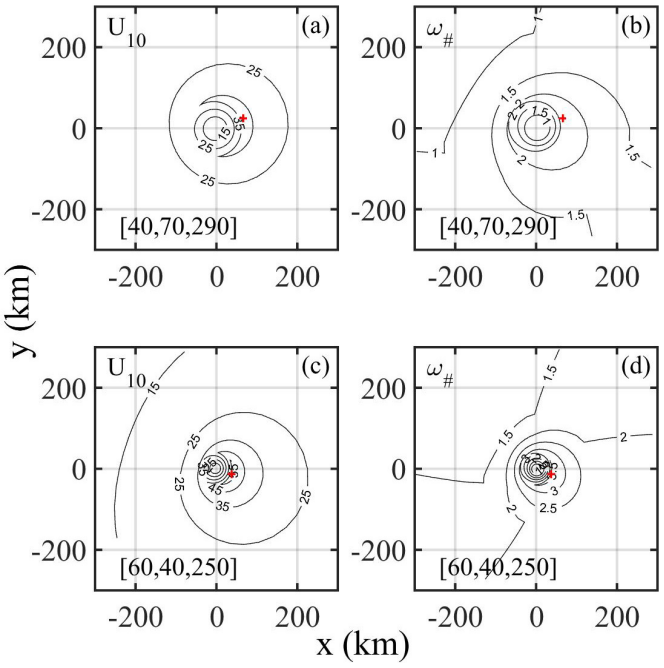

Fig. 6. Examples of the [Left column (a) and (c)] U_{10} and [Right column (b) and (d)] $\omega_\#$ fields calculated with the parametric models described in Section III. The hurricane parameters [U_{10m}, r_m, ϕ_m] are (Top row) [40, 70, 280°] and (Bottom row) [60, 40, 250], $a_{1U} = 0.1$ for both cases. (a) and (c) U10. (b) and (d) $\omega_\#$.

Fig. 6 shows two examples of the 2-D fields of U_{10} (left column) and $\omega_\#$ (right column) generated by the parametric models: (7) and (8) for the former and (3)–(6) for the latter, with $a_{1U} = 0.1$. The hurricane parameters [U_{10m}, r_m, ϕ_m] used for the computation are shown in the square brackets at the lower left corner of each panel. The hurricane heading is toward the top of the figure, and the location of maximum wind speed is shown with a red plus marker. The computed 2-D fields provide a reasonable representation of the asymmetric U_{10} and $\omega_\#$ distributions inside hurricanes as observed from the wind and wave measurements obtained in hurricane reconnaissance and research missions [6], [18]–[22].

IV. Low-Pass-Filtered Mean-Square Slopes Inside Hurricanes

With U_{10} and $\omega_\#$ given by the parametric models, the spectral slope $-s$ becomes the only remaining free parameter in the spectral function for LPMSS computation. Through numerical experimentation matching MSS_{k10} with the MSS_{GPS} data shown in Fig. 2 using the parametric U_{10} and $\omega_\#$ fields, we search for a simple formula relating s and U_{10}.

Fig. 7 shows two examples computed with the empirical $s(U_{10})$ relationship

$$s = \begin{cases} s_1, & U_{10} \le U_1 \\ s_1(U_{10}/U_1)^q, & U_{10} > U_1. \end{cases} \tag{9}$$

The parameters [s_1, U_1, q] = [4.7, 18, 1/8] and [4.65, 15, 1/9] are used for Fig. 7(a) and (b), respectively. The hurricane parameters [U_{10m}, r_m, a_{1U}, ϕ_m] = [40, 70, 0.1, 280°] are used for the computation. The U_{10} and $\omega_\#$ fields are calculated with 5-km radial resolution for r = 0–200 km,

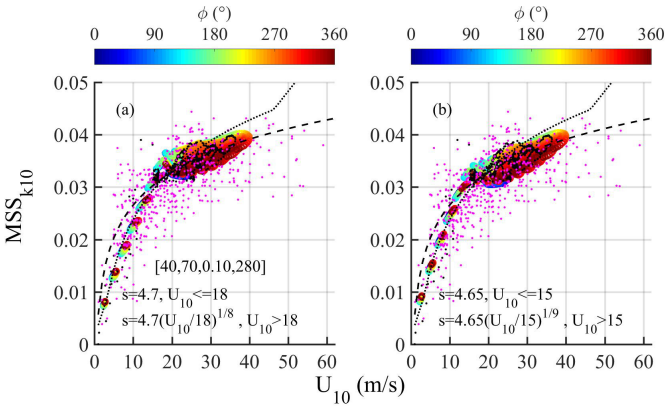

Fig. 7. $\mathrm{MSS_{GPS}}$ measurements are used to establish an empirical relation of $s(U_{10})$: (9). (a) $[s_1, U_1, q] = [4.7, 18, 1/8]$. (b) $[s_1, U_1, q] = [4.65, 15, 1/9]$. The hurricane parameters $[U_{10m}, r_m, a_{1U}, \phi_m]$ are [40, 70, 0.1, 280]. The model computed MSS_{k10} is shown with circles color-coded with ϕ; the $\mathrm{MSS_{GPS}}$ is shown with dots: magenta for K0913 and black for G1318.

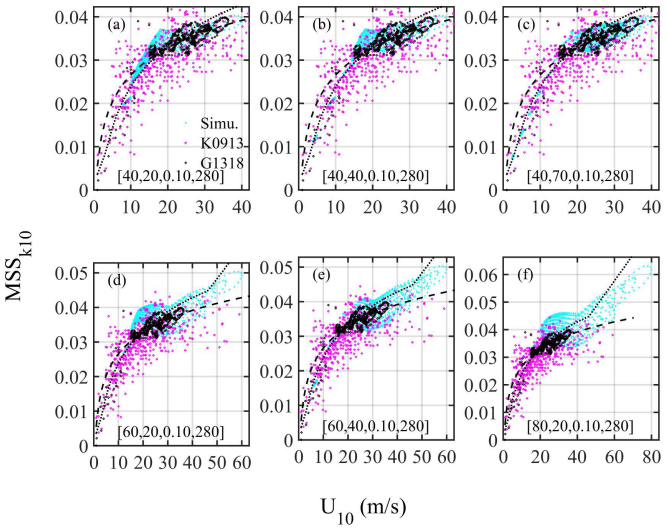

Fig. 8. Examples showing the MSS_{k10} sensitivity to U_{10m} and r_m. The hurricane parameters $[U_{10m}, r_m, a_{1U}, \phi_m]$ are listed at the bottom of each panel. The model results are shown with cyan markers; the $\mathrm{MSS_{GPS}}$ is shown with dots: magenta for K0913 and black for G1318. (a)–(c) Only r_m is varied from 20 to 70 km. The results indicate a relatively insignificant effect of r_m on the MSS_{k10} computation. (d)–(f) Stronger response to U_{10m} variation.

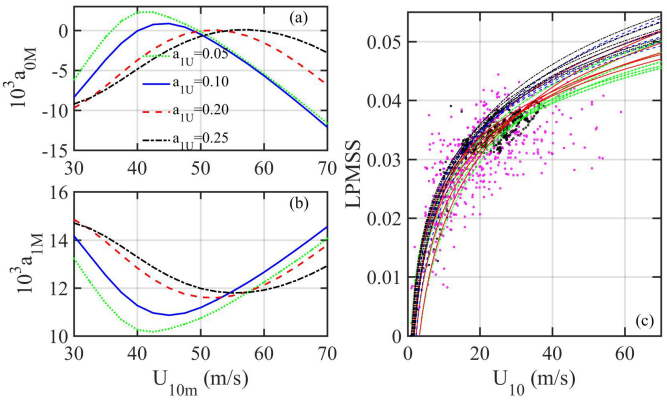

Fig. 9. MSS_{k10} sensitivity to a_{1U} for a range of U_{10m}. The results are presented with the coefficients of the fit logarithmic function of MSS_{k10} (U_{10}) given in (10). (a) a_{0M} versus U_{10m}. (b) a_{1M} versus U_{10m}. (c) LPMSS dependence on U_{10}: the $\mathrm{MSS_{GPS}}$ is shown with dots: magenta for K0913 and black for G1318, the fit curves for the modeled results are shown with smooth curves; computations with $a_{1U} = 0.05$, 0.1, 0.2, and 0.25 are illustrated, respectively, with green, blue, red, and black curves.

and 10° azimuthal resolution for $\phi = 0°$–$360°$. The plotted MSS_{k10} is color-coded with respect to the azimuth angle as shown in the color bar. The $\mathrm{MSS_{GPS}}$ data are plotted with small dots: magenta for K0913 [7], [8] and black for G1318 [9], [10]. The superimposed dotted and dashed lines are the LPMSS(U_{10}) equations: labeled K06 and G18 from [7] and [10], respectively. The two sets of $[s_1, U_1, q]$ produce almost identical outcome of the LPMSS computation. The results in the remainder of this paper are based on $[s_1, U_1, q] = [4.7, 18, 1/8]$. It is found that the azimuthal or radial dependence of the resulting MSS_{k10} is rather weak (Fig. 7), so the concluding results derived from this paper are suitable for single transects such as those encountered in the GPS reflectometry application.

Fig. 8 illustrates the U_{10m} and r_m sensitivity of the computed MSS_{k10} ($a_{1U} = 0.1$). On the top row, r_m is varied [20, 40, and 70 km for Fig. 8(a)–(c)], with U_{10m} and ϕ_m fixed (40 m/s and 280°). The model-generated MSS_{K10} is shown with cyan pluses, and the data and empirical formulas of $\mathrm{MSS_{GPS}}$ are superimposed with the same markers and line types as those used in Fig. 7. The impact of varying r_m appears to be rather minor.

The lower row of Fig. 8, combined with Fig. 8(a) and (b), shows the results of varying U_{10m}; the hurricane parameters $[U_{10m}, r_m, \phi_m]$ are [60, 20, 280], [60, 40, 280], and [80, 20, 280] for Fig. 8(d)–(f), respectively. The MSS_{k10} wind speed dependence shows noticeable variation with varying U_{10m}, in contrast to the results from varying r_m [compare Fig. 8 top row versus Fig. 8(a), (d), and (f), or Fig. 8(b) and (e)].

The effect of varying various hurricane parameters is further investigated with U_{10m} varying from 30 to 80 m/s, and a_{1U} varying between 0.05 and 0.25. The r_m and ϕ_m are fixed at 40 km and 280°, respectively; the computed MSS_{k10} is fit with the logarithmic function

$$\mathrm{MSS}_{k10} = a_{0M} + a_{1M} \ln(U_{10}). \tag{10}$$

Fig. 9(a) and (b) presents the resulting a_{0M} and a_{1M} as functions of U_{10m}. The computations with $a_{1U} = 0.05$, 0.1, 0.2, and 0.25 are shown with green, blue, red, and black lines, respectively. The fit curves of $\mathrm{MSS}_{k10}(U_{10})$ for $U_{10m} = 30$–80 m/s are shown in Fig. 9(c) with the same set of line colors as those in Fig. 9(a) and (b). The $\mathrm{MSS_{GPS}}$ data sets are superimposed (magenta dots for K0913 and black dots for G1318). For a given wind speed, the computed results vary within a small range (about ±15% in low winds and ±10% in high winds) for various degrees of wind field asymmetry denoted by a_{1U}, and the computed MSS_{k10} is in reasonably good agreement with the $\mathrm{MSS_{GPS}}$ observations over the full range of wind speed.

In many microwave remote sensing computations, it is necessary to define the crosswind and upwind components of the MSS: s_c^2 and s_u^2, respectively. The artificial slick data set of Cox and Munk [16] remains the most comprehensive field

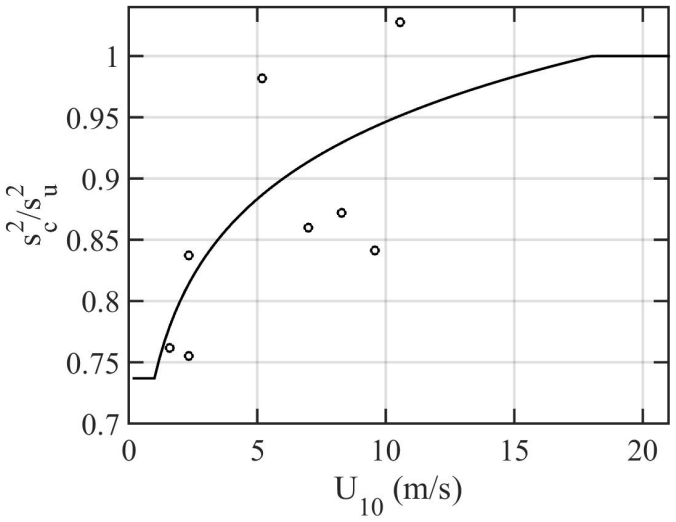

Fig. 10. Ratio between crosswind and upwind components of the LPMSS derived from airborne sun glitter measurements in slicked waters [16]; the recommended wind speed dependence function (11) is shown in the solid curve.

measurements of LPMSS with crosswind and upwind resolution. The ratio $R_{\rm cu} = s_c^2/s_u^2$ shows a logarithmic dependence on U_{10} (Fig. 10) with the magnitude in the measurements distributed over a narrow range between about 0.75 and 1.03. Further discussions on the directional properties of ocean surface roughness have been given in [24]. It is reasonable to set unity as the upper bound of the expected $R_{\rm cu}$. The unity upper bound corresponds to an isotropic surface roughness distribution in the chaotic sea generated by high winds. The following function is recommended based on least-squares fitting of the artificial slick data set of Cox and Munk [16]

$$R_{\rm cu} = \begin{cases} 0.737, & U_{10} \le 1 \text{ m/s} \\ 0.737 + 0.091 \ln U_{10}, & 1 < U_{10} \le 18 \text{ m/s} \\ 1, & U_{10} > 18 \text{ m/s}. \end{cases} \quad (11)$$

V. Summary

Ocean surface waves are the roughness elements for microwave remote sensing of the ocean environments. With lower microwave frequencies, the influence of the spectral components in the energetic dominant wave region becomes increasingly important. Extensive researches have devoted to the wind wave spectral models focusing on the dominant wave region [1]–[6]. It is well established that the wave spectrum is not only dependent on the wind speed but also on the wave age, which is the inverse dimensionless spectral peak frequency $\omega_\#$. For wind waves, $\omega_\#$ can be represented by an equivalent dimensionless fetch or duration [2]–[6], [24], [25]. Many wind wave spectral models have been designed with the above considerations with three key spectral coefficients α, σ, and γ expressed as functions of $\omega_\#$, further detail is given in [6], and a summary is provided in the Appendix.

The spectral slope for the high-frequency region prescribed in earlier wind wave spectral models is either -4 or -5. Whereas the effect of s on the surface height determination is minor, its impact on the MSS estimation is significant (Figs. 1 and 2). The recent development of a general (G) spectral model that accommodates variable s in the spectral function as well as the associated spectral coefficients α, σ, and γ permits us to explore quantitatively the impact of s on the LPMSS computation.

The elevated interest for ocean remote sensing using the reflectometry technique with microwave sources from existing GPS or other communication satellites has generated many data sets of LPMSS collected in a wide range of wind and wave conditions. Taking advantage of the similarity relations of the hurricane wind and wave fields, we have developed parametric models for the spatial distributions of U_{10} and $\omega_\#$ inside hurricanes (Section III, Figs. 3–6). With the 2-D fields of U_{10} and $\omega_\#$ inside hurricanes provided by the parametric models, the $\rm MSS_{GPS}$ data collected inside hurricanes [7]–[10] are used to establish a wind speed function for s [Fig. 7, (9)].

The parametric models of U_{10} and $\omega_\#$ coupled with the $s(U_{10})$ function are then used to study the sensitivity of LPMSS(U_{10}) relationship with respect to key hurricane parameters U_{10m}, r_m, a_{1U}, and ϕ_m (Figs. 8 and 9). The modeled $\rm MSS_{k10}$ shows good agreement with field measurements of $\rm MSS_{GPS}$, and both display the same logarithmic wind speed dependence [Figs. 7–9, (10)]. Finally, an empirical formula [Fig. 10, (11)] for the ratio between the crosswind and upwind components of the LPMSS is obtained using the airborne sun glitter observations in artificial slick waters reported in [16].

In the future, it would be very interesting to compare the predictions of the results from the parametric models with those of numerical models such as WW3. Hurricane wind and wave fields are complicated; for example, reference [26] identifies no less than 11 similarly important mechanisms shaping the wave field inside the hurricane. So, a legitimate question arises: how all of these boils down to just a variable fetch (or equivalently $\omega_\#$) and the spectral slope s?

The answer may be found by recognizing several remarkable similarity relationships.

1) For deep-water wind-generated waves, the wave spectrum is uniquely determined by the U_{10} and $\omega_\#$ (Appendix).
2) Despite the violent mode of creation, the waves inside hurricanes adhere to the fetch- and duration-limited nature of wind wave generation [18]–[20]. Furthermore, the U_{10} and $\omega_\#$ fields can be described reasonably well by simple parametric models (Section III) with just a few key TC parameters (U_{10m}, r_m, ϕ_m, and a_{1U} top the list). The dominant wave properties inside TCs can thus be defined reasonably well by a few key TC parameters.
3) Although not important to determining the dominant wave properties, the spectral slope $-s$ is critical to quantifying the LPMSS.
4) The recent compilation of $\rm MSS_{GPS}$ over a wide range of wind and wave conditions provides the needed information to establish a functional relationship between s and wind speed.
5) And finally, numerical experiments through the U_{10} and $\omega_\#$ parametric model computations indicate the relative insensitivity of many key TC parameters, and the logarithmic wind speed dependence of LPMSS is very robust [Figs. 7–9, (10)]. This information is

useful for tasks such as EM forward computation and experiment design.

APPENDIX
MATHEMATICAL FORMULAS FOR THE WIND WAVE SPECTRAL MODELS

The P model [1] is given as

$$S(\omega) = \alpha_P g^2 \omega^{-5} \exp\left[-\beta_P \left(\frac{\omega}{\omega_0}\right)^{-4}\right] \tag{A1}$$

where $\alpha_P = 8.10 \times 10^{-3}$, $\beta_P = 0.74$, $\omega_0 = g/U_{19.5}$, and $U_{19.5}$ is the wind speed measured on the weather ship with the sensor elevation at 19.5 m above mean sea level. To use U_{10} as the reference wind speed, the ratio $U_{19.5}/U_{10} = 1.08$ can be applied; this approximation is based on the mean and standard deviation of the $U_{19.5}/U_{10}$ ratios (1.08 and 0.02) setting the dynamic roughness z_0 between 10^{-4} and $10^{-1.5}$ in the logarithmic wind speed profile $U_z/u_* = (1/\kappa)\ln(z/z_0)$, where z is the sensor height, u_* is the wind friction velocity, and $\kappa = 0.4$ is the von Kármán constant. Dropsonde data have shown that the logarithmic wind speed profile remains a good representation of the vertical distribution of wind speed in the lower surface boundary layer of the hurricane wind field [27], [28].

The J model [2], [3] is given as

$$S(\omega) = \alpha_J g^2 \omega^{-5} \exp\left[-\frac{5}{4}\left(\frac{\omega}{\omega_p}\right)^{-4}\right] \gamma_J^{\Gamma_J}$$

$$\Gamma_J = \exp\left[-\frac{(\omega-\omega_p)^2}{2\sigma_J^2\omega_p^2}\right] \tag{A2}$$

where ω_p is the spectral peak frequency, and α_J is no longer a constant but varies with the wind fetch x_f

$$\alpha_J = 0.076 x_\#^{-0.22} \tag{A3}$$

where $x_\# = x_f g U_{10}^{-2}$ is the dimensionless fetch. The dependence on fetch can be converted to the dependence on wave age ($c_p/U_{10} = 1/\omega_\#$, where c_p is the wave phase speed of the spectral peak component). Using their wave frequency growth function: $\omega_\# = 21.99 x_\#^{-0.33}$, (A3) can be rewritten as

$$\alpha_J = 9.88 \times 10^{-3} \omega_\#^{0.66}. \tag{A4}$$

The two peak enhancement parameters γ_J and σ_J are also expected to depend on dimensionless fetch or wave age, but the JONSWAP data scatter is very large. In practice, the mean values $\gamma_J = 3.3$, $\sigma_a = 0.07$, and $\sigma_b = 0.09$ are frequently employed. (The J model defines the peak width σ_J as σ_a and σ_b for $\omega < \omega_p$ and $\omega \geq \omega_p$, respectively.)

After reviewing more than a dozen data sets, Hasselmann *et al.* [3] suggest the power function dependence for the spectral coefficients. From the average values listed in the last entry of [3, Table 1], the following formulas are derived:

$$\alpha_{J2} = 7.33 \times 10^{-3} \omega_\#^{0.87} \tag{A5}$$

$$\gamma_{J2} = 2.29 \omega_\#^{0.32} \tag{A6}$$

$$\sigma_{aJ2} = 9.85 \times 10^{-2} \omega_\#^{-0.32} \tag{A7}$$

$$\sigma_{bJ2} = 1.05 \times 10^{-1} \omega_\#^{-0.16}. \tag{A8}$$

The D model [4] is given as

$$S(\omega) = \alpha_D g^2 \omega_p^{-1} \omega^{-4} \exp\left[-\left(\frac{\omega}{\omega_p}\right)^{-4}\right] \gamma_D^{\Gamma_D}$$

$$\Gamma_D = \exp\left[-\frac{(\omega-\omega_p)^2}{2\sigma_D^2\omega_p^2}\right]. \tag{A9}$$

The spectral coefficients obtained from their data are

$$\alpha_D = 0.006 \omega_\#^{0.55}; \quad 0.83 < \omega_\# < 5 \tag{A10}$$

$$\gamma_D = \begin{cases} 1.7, & 0.83 < \omega_\# < 1 \\ 1.7 + 6.0 \log \omega_\#, & 1 \leq \omega_\# < 5 \end{cases} \tag{A11}$$

$$\sigma_D = 0.08(1 + 4\omega_\#^{-3}); \quad 0.83 < \omega_\# < 5. \tag{A12}$$

The Y model [5] is given as

$$S(\omega) = \alpha_Y g^2 \omega_p^{-(5+s)} \omega^{-s} \exp\left[-\frac{s}{4}\left(\frac{\omega}{\omega_p}\right)^{-4}\right] \gamma_Y^{\Gamma_Y}$$

$$\Gamma_Y = \exp\left[-\frac{(\omega-\omega_p)^2}{2\sigma_Y^2\omega_p^2}\right]. \tag{A13}$$

Young [5] does not resolve the spectral slope dependence of the associated spectral coefficients α_Y, γ_Y, and σ_Y, so its legitimate application is still restricted to $s = 4$ or 5 using the (α, γ, σ) by Donelan *et al.* [4] or Hasslemann *et al.* [2], [3], thus resulting in identical outcome as that of the D or J model.

The G model [6] also accepts a variable spectral slope and is given as

$$S(\omega) = \alpha_G g^2 \omega_p^{-5} \varsigma^{-s} \exp\left[-\left(\frac{\varsigma}{K}\right)^{-\beta_G}\right] \gamma_G^{\Gamma_G}$$

$$\Gamma_G = \exp\left[-\frac{(1-\varsigma)^2}{2\sigma_G^2}\right]; \quad \varsigma = \frac{\omega}{\omega_p} \tag{A14}$$

where K is a scaling factor such that the peak of $S(\omega)$ is at ω_p. Setting $dS/d\omega = 0$, one obtains $K = (s/\beta_G)^{1/\beta_G}$. In the G model, the associated spectral coefficients vary with s as detailed in the following; the spectral slope at the high-frequency portion is no longer restricted to -4 or -5. The P, J, D, and Y models are subsets of the G model, i.e., for the P model, [s, β_G, γ_G] = [5, 4, 1]; for the J model, [s, β_G] = [5, 4]; for the D model, [s, β_G] = [4, 4]; and for the Y model, [β_G] = [4].

In practical application, it turns out that the impact of varying β_G in (A14) is relatively small in comparison to varying α_G, γ_G, and σ_G. Furthermore, the nonlinear curve fitting procedure becomes more complicated as the number of fitting variables increases, thus placing higher demand on the quality and quantity of wave spectra used for analysis. Limited by the spectral resolution and data quality in high-frequency region, $\beta_G = 4$ is adopted following the examples of the P, J, D, and Y models. From this point, the subscript letters associated with α, γ, and σ for different models are dropped unless clarification is necessary.

The spectral coefficients for the G model are estimated in two steps. The first step uses the combined data of spectral coefficients processed from the wave spectra measured during an air–sea interaction experiment (INTOA) in the Gulf of Tehuantepec, Mexico, [13]–[15] with the published results of

JONSWAP [2], [3] and Donelan *et al.* [4]. This combination is necessary because the INTOA $\omega_\#$ range is rather limited: from 1.4 to 3.3 for $U_{10} > 7$ m/s, but mostly between 1.5 and 2.7. The combined data yield

$$\alpha_1 = A_\alpha \omega_\#^{a_\alpha} \tag{A15}$$

$$\gamma_1 = A_\gamma + a_\gamma \log(\omega_\#) \tag{A16}$$

$$\sigma_1 = A_\sigma + a_\sigma \log(\omega_\#). \tag{A17}$$

The coefficients $A_\alpha, a_\alpha, A_\gamma, a_\gamma, A_\sigma$, and a_σ are the functions of s

$$\begin{aligned} A_\alpha &= 1.30 \times 10^{-3} s + 1.64 \times 10^{-3} \\ a_\alpha &= 4.83 \times 10^{-1} s - 1.49 \\ A_\gamma &= 4.42 \times 10^{-1} s + 3.93 \times 10^{-1} \\ a_\gamma &= -3.63 s + 19.74 \\ A_\sigma &= -5.39 \times 10^{-2} s + 3.44 \times 10^{-1} \\ a_\sigma &= 2.05 \times 10^{-9} s + 5.5 \times 10^{-2}. \end{aligned} \tag{A18}$$

In the second step, the wind wave growth function $\eta_\#(\omega_\#)$ is used to refine the parameters to expand the application range in $\omega_\#$. The analysis leads to

$$\alpha_G = \alpha_1[1 - 0.3 \tanh(0.1\omega_\#)] \tag{A19}$$

$$\gamma_G = \gamma_1[1 - 0.5 \tanh(0.1\omega_\#)]. \tag{A20}$$

The spectral parameter σ_G was left in the same form as defined in (A17) and (A18) due to its large data scatter in the available data sources, i.e., $\sigma_G = \sigma_1$ (A17).

ACKNOWLEDGMENT

The authors would like to thank E. Walsh for providing the wind and wave data and the HRD wind archive maintained in the HWIND legacy data site http://www.rms.com/perils/hwind/legacy-archive/. Data sets used in this analysis are given in the references cited. The processing codes and data segments can also be obtained by contacting the corresponding author. A MATLAB code package is deposited at https://www.researchgate.net/publication/325315052_HurrSimilaryRelationshipsCodePackage.

REFERENCES

[1] W. J. Pierson, Jr., and L. Moskowitz, "A proposed spectral form for fully developed wind seas based on the similarity theory of S. A. Kitaigorodskii," *J. Geophys. Res.*, vol. 69, no. 24, pp. 5181–5190, 1964.

[2] K. Hasselmann *et al.*, "Measurements of wind-wave growth and swell decay during the Joint North Sea Wave Project (JONSWAP)," *Deutches Hydrographisches Inst.*, vol. A8, no. 12, pp. 1–95, 1973.

[3] K. Hasselmann, D. B. Ross, P. Müller, and W. Sell, "A parametric wave prediction model," *J. Phys. Oceanogr.*, vol. 6, no. 3, pp. 200–228, Mar. 1976.

[4] M. A. Donelan, J. Hamilton, and W. H. Hui, "Directional spectra of wind-generated ocean waves," *Philos. Trans. Roy. Soc. London A, Math. Phys. Sci.*, vol. A315, no. 1534, pp. 509–562, Sep. 1985.

[5] I. R. Young, "Directional spectra of hurricane wind waves," *J. Geophys. Res.*, vol. 111, no. C8, pp. C08020-1–C08020-14, Aug. 2006.

[6] P. A. Hwang, Y. Fan, F. J. Ocampo-Torres, and H. García-Nava, "Ocean surface wave spectra inside tropical cyclones," *J. Phys. Oceanogr.*, vol. 47, no. 10, pp. 2293–2417, Oct. 2017.

[7] S. J. Katzberg and J. Dunion, "Comparison of reflected GPS wind speed retrievals with dropsondes in tropical cyclones," *Geophys. Res. Lett.*, vol. 36, pp. L17602-1–L17602-5, Sep. 2009, doi: 10.1029/2009GL039512.

[8] S. J. Katzberg, J. Dunion, and G. G. Ganoe, "The use of reflected GPS signals to retrieve ocean surface wind speeds in tropical cyclones," *Radio Sci.*, vol. 48, pp. 371–387, Jul. 2013, doi: 10.1002/rds.20042.

[9] S. Gleason, "Space-based GNSS scatterometry: Ocean wind sensing using an empirically calibrated model," *IEEE Trans. Geosci. Remote Sens.*, vol. 51, no. 9, pp. 4853–4863, Sep. 2013.

[10] S. Gleason *et al.*, "Study of surface wind and mean square slope correlation in hurricane Ike with multiple sensors," *IEEE J. Sel. Topics Appl. Earth Observ. Remote Sens.*, vol. 11, no. 6, pp. 1975–1988, Jun. 2018, doi: 10.1109/JSTARS.2018.2827045.

[11] P. A. Hwang and F. Fois, "Surface roughness and breaking wave properties retrieved from polarimetric microwave radar backscattering," *J. Geophys. Res.*, vol. 120, no. 5, pp. 3640–3657, May 2015.

[12] I. R. Young, "Observations of the spectra of hurricane generated waves," *Ocean Eng.*, vol. 25, nos. 4–5, pp. 261–276, Dec. 1998.

[13] F. J. Ocampo-Torres, H. García-Nava, R. Duranzo, P. Osuna, G. M. D. Méndez, and H. C. Graber, "The intOA experiment: A study of ocean-atmosphere interactions under moderate to strong offshore winds and opposing swell conditions in the gulf of Tehuantepec, Mexico," *Boundary-Layer Meteorol.*, vol. 138, no. 3, pp. 433–451, 2011.

[14] H. García-Nava, F. J. Ocampo-Torres, P. Osuna, and M. A. Donelan, "Wind stress in the presence of swell under moderate to strong wind conditions," *J. Geophys. Res.*, vol. 114, pp. C12008-1–C12008-12, Dec. 2009, doi: 10.1029/2009JC005389.

[15] P. A. Hwang, H. García-Nava, and F. J. Ocampo-Torres, "Observations of wind wave development in mixed seas and unsteady wind forcing," *J. Phys. Oceanogr.*, vol. 41, no. 12, pp. 2343–2362, Dec. 2011, doi: 10.1175/JPO-D-11-044.1.

[16] C. Cox and W. Munk, "Statistics of the sea surface derived from sun glitter," *J. Marine Res.*, vol. 13, no. 2, pp. 198–227, 1954.

[17] S. J. Katzberg, O. Torres, and G. Ganoe, "Calibration of reflected GPS for tropical storm wind speed retrievals," *Geophys. Res. Lett.*, vol. 33, pp. L18602-1–L18602-5, Sep. 2006, doi: 10.1029/2006GL026825.

[18] P. A. Hwang, "Fetch- and duration-limited nature of surface wave growth inside tropical cyclones: With applications to air–sea exchange and remote sensing," *J. Phys. Oceanogr.*, vol. 46, no. 1, pp. 41–56, Jan. 2016.

[19] P. A. Hwang and E. J. Walsh, "Azimuthal and radial variation of wind-generated surface waves inside tropical cyclones," *J. Phys. Oceanogr.*, vol. 46, no. 9, pp. 2605–2621, Sep. 2016, doi: 10.1175/JPO-D-16-0051.1.

[20] P. A. Hwang and Y. Fan, "Effective fetch and duration of tropical cyclone wind fields estimated from simultaneous wind and wave measurements: Surface wave and air-sea exchange computation," *J. Phys. Oceanogr.*, vol. 47, no. 2, pp. 447–470, Feb. 2017, doi: 10.1175/JPO-D-16-0180.1.

[21] G. J. Holland, "An analytic model of the wind and pressure profiles in hurricanes," *Monthly Weather Rev.*, vol. 108, no. 8, pp. 1212–1218, Aug. 1980.

[22] G. J. Holland, J. I. Belanger, and A. Fritz, "A revised model for radial profiles of hurricane winds," *Monthly Weather Rev.*, vol. 136, no. 9, pp. 4393–4401, Sep. 2010.

[23] P. A. Hwang and D. W. Wang, "Directional distributions and mean square slopes in the equilibrium and saturation ranges of the wave spectrum," *J. Phys. Oceanogr.*, vol. 31, no. 5, pp. 1346–1360, May 2001.

[24] P. A. Hwang and D. W. Wang, "Field measurements of duration-limited growth of wind-generated ocean surface waves at young stage of development," *J. Phys. Oceanogr.*, vol. 34, no. 10, pp. 2316–2326, Oct. 2004.

[25] P. A. Hwang, "Duration- and fetch-limited growth functions of wind-generated waves parameterized with three different scaling wind velocities," *J. Geophys. Res.*, vol. 111, no. 2, pp. C02005-1–C02005-10, Feb. 2006, doi: 10.1029/2005JC003180.

[26] M. A. Donelan, M. Curcic, S. S. Chen, and A. K. Magnusson, "Modeling waves and wind stress," *J. Geophys. Res.*, vol. 117, no. 2, pp. C00J23-1–C00J23-26, Jul. 2012, doi: 10.1029/2011JC007787.

[27] M. D. Powell, P. J. Vickery, and T. A. Reinhold, "Reduced drag coefficient for high wind speeds in tropical cyclones," *Nature*, vol. 422, pp. 279–283, Mar. 2003.

[28] J. L. Franklin, M. L. Black, and K. Valde, "GPS dropwindsonde wind profiles in hurricanes and their operational implications," *Weather Forecasting*, vol. 18, no. 2, pp. 32–44, Mar. 2003.

Paul A. Hwang received the B.S. degree in oceanography from National Taiwan Ocean University, Keelung, Taiwan, in 1973, the M.S. degree in ocean engineering from The University of Rhode Island, Kingston, RI, USA, in 1978, and the Ph.D. degree in civil engineering from the University of Delaware, Newark, DE, USA, in 1982.

He had two and half years post-doctoral training at the Air-Sea Interaction Laboratory, University of Delaware. He was a Staff Scientist for four years at Ocean Research and Engineering, Pasadena, CA, USA, one year at Science and Technology, Hampton, VA, USA, and five years at Quest Integrated, Inc., Kent, WA, USA. He was with the Oceanography Division, U.S. Naval Research Laboratory, from 1995 to 2006, where he has been with the Remote Sensing Division since 2006. His research interests include spatial and temporal evolution of ocean surface waves, characteristics of ocean surface roughness, and hydrodynamic aspects of microwave and acoustic remote sensing of the ocean.

Yalin Fan received the B.S. degree in oceanography from Ocean University of China, Qingdao, China, in 1995, the M.S. degree in oceanography from the University of New Hampshire, Durham, NH, USA, in 2000, and the Ph.D. degree in oceanography, The University of Rhode Island (URI), Narragansett, RI, USA, in 2007.

She was an Oceanography Technician with the University of Massachusetts Dartmouth, Dartmouth, MA, USA, from 2001 to 2003. She was a Marine Research Associate with URI from 2007 to 2009 and an Associate Research Scholar with Princeton University, Princeton, NJ, USA, from 2010 to 2013. She was a Post-Doctoral Researcher with the U.S. Naval Research Laboratory from 2013 to 2015, where she has been an Oceanographer since 2015. Her research interests include air-sea interaction, momentum and heat exchange across the air-sea interface, surface gravity waves, Langmuir turbulence, wave modeling, numerical model coupling, large eddy circulation modeling, and ocean turbulence.